OE Optical Engineering

RESEARCH PAPER

Haze reduction in concentric electrode-based large aperture liquid crystal lens with segmented phase profile

Amit K. Bhowmick,[a] Afsoon Jamali,[b] Douglas Bryant,[a] Sandro Pintz,[b] and Philip J. Bos[a,*]

[a]Kent State University, Material Science Graduate Program, Kent, Ohio, United States
[b]Meta Platforms Inc., Reality Labs, Redmond, Washington, United States

ABSTRACT. In the field of augmented reality/virtual reality head-mounted displays or eyeglasses, electro-optical tunable lenses have great potential to resolve the issue of accommodation-convergence conflicts and to correct vision problems. A high-quality tunable lens with a large field of view is highly desired for these near-to-eye applications. Recently, gradient refractive index tunable liquid crystal lenses with a concentric ring electrode design and segmented phase profile have received attention due to their compactness, low-voltage requirement, and ability to provide a large aperture size while maintaining a fast-switching speed. However, this design can result in degradation of optical quality, causing haze from the phase reset boundaries and electrode discontinuity. We analyze the cause of haze and presents solutions to reduce these effects, and we experimentally validate them.

Keywords: electroptics; tunable lens; augmented reality/virtual reality; liquid crystals

Paper 20230300G received Mar. 31, 2023; revised Jul. 5, 2023; accepted Jul. 14, 2023; published Aug. 4, 2023.

1 Introduction

Large aperture tunable lenses have recently gained interest for near-to-eye applications, such as in the field of augmented reality (AR)/virtual reality (VR) to correct accommodation-convergence (AC) mismatch issues[1–8] and wearable eyeglass applications to correct human vision problems.[9–12] In current head-mounted displays (HMDs), for the VR application, a physical display is placed behind a fixed power magnifying lens. The role of the fixed power magnifying lens is to create a virtual image at a fixed distance, where the human eye accommodates. This fixed distance is called the accommodation distance. To sense the depth of virtual images, stereoscopic images are presented to the viewer's eyes to cause their vergence angle to adjust to be the same as it would be for an actual object at the depth of the presented computer generated one. However, although the vergence angle of the eyes provides a cue as to the depth of the virtual object, the focus cue is fixed and does not provide the appropriate depth cue as it would for a real-world object. This results in a cue conflict known as the AC mismatch, which causes eyestrain and an unnatural user experience.[4,8] The solution of AC mismatch will help to create a real-world stereographic sense of depth; hence, the eye fatigue issue of using HMDs will be significantly reduced. Among various techniques to solve the AC mismatch problem,[13–16] the use of tunable lenses has drawn attention recently.

*Address all correspondence to Philip J. Bos, pbos@kent.edu

There are many approaches have been proposed in past years to demonstrate tunable focus lenses, e.g., Alvarez lenses,[17] electrowetting lenses,[18] dielectrophoretic lenses,[19] fluid-filled lenses,[20,21] and liquid crystal (LC) lenses.[22–26] However, tunable lenses that have a large diameter (>1 cm) always faced challenges related to size, weight, shape, speed, power consumption, and optical quality. After reviewing the prospects of various techniques to resolve the AC mismatch in HMDs, Kramida[27] concluded that tunable LC lenses coupled with an eye-tracking system have the highest potential to solve the AC mismatch problem. Lin et al.[28] reviewed all available tunable LC lens technologies. For excellent control of the tunable phase profile, the concentric ring electrode-based LC lens has been widely studied.[29–33]

An LC is a birefringent material with an extraordinary refractive index (n_e) for light polarized along the long average molecular axis and ordinary refractive index (n_o) along the short average molecular axis. In nematic LC-based lenses, the LC material is sandwiched between two glass substrates that are separated by thickness d. The inner layer of the substrates has a transparent conductive layer with a coated polymer alignment layer. The alignment layer orients the LC director along a defined axis (rubbing direction) when no voltage is applied (Y axis). If we consider that the LC director lies within the $Y-Z$ plane when an electric field is applied along the Z axis, the effective refractive index for light polarized along the Y axis for a director orientation angle θ, shown in Fig. 1(a), is written as follows:

$$n_{e,\text{effective}} = \frac{n_o n_e}{\sqrt{n_e^2 \cos^2(\theta) + n_o^2 \sin^2(\theta)}}. \tag{1}$$

The effective value of $n_{e,\text{effective}}$ varies from n_o to n_e, so the maximum optical path difference (OPD) for the case of the director angle varying from 0 deg to 90 deg is written as follows:

$$\text{OPD}_{\text{LC}} = (n_e - n_0)d. \tag{2}$$

The OPL(r) of an ideal lens (of maximum radius R and focal length f) that follows parabolic phase profile is expressed as follows:

$$\text{OPL}(r)_{\text{ideal negative lens}} = \frac{r^2}{2f}, \tag{3a}$$

$$\text{OPL}(r)_{\text{ideal positive lens}} = \frac{(R^2 - r^2)}{2f}. \tag{3b}$$

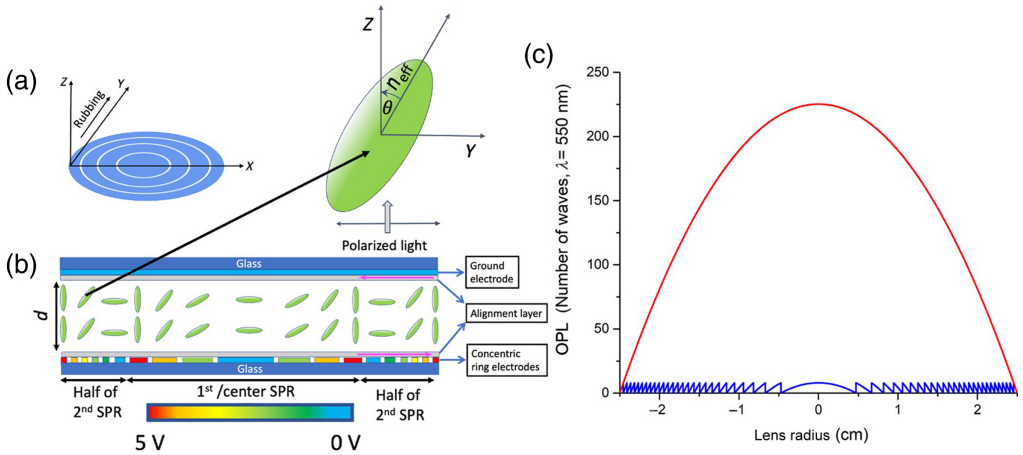

Fig. 1 (a) Concentric ring electrodes diagram in 3D coordinates. (b) Schematic diagram of the side view (in $Y-Z$ plane) of the LC director orientation in a concentric electrode-based SPP design LC lens within the first two SPRs. The green ellipses represent the LC molecules under voltage application, the pink arrow represents the rubbing direction, and the color bar shows the value of the voltage on the electrodes. (c) Phase profile of an example SPP LC lens compared with the continuous parabolic phase-based lens: the red curve shows the OPL of a refractive lens with an optical power of +0.40 D, and the blue curve shows the OPL profile of example 5 cm diameter SPP LC lens with 28 segmented phase resets to achieve a +0.40 D optical power.

Notice that the maximum OPD between the center and edge of an ideal lens is then

$$\mathrm{OPD}(R)_{\text{ideal lens}} = \frac{R^2}{2f}. \tag{3c}$$

As given by Eq. (3), the effective refractive index for the LC cell needs to change in parabolic fashion. Such a gradient refractive index (GRIN) change can be achieved by concentric ring electrodes, with the widths of the discrete electrodes varying in parabolic fashion from the center toward the edge of the lens. With proper voltage distribution on the discrete electrodes, the phase profile within the entire aperture can be controlled. For a specific sampling rate f_s (number of phase step per wave), the total number of discrete electrodes (N_e) is calculated from the following equation:

$$N_e = \mathrm{OPD}_{\text{ideal lens}} \times \frac{f_s}{\lambda}. \tag{4}$$

A near-diffraction limited LC lens based on a concentric ring electrode was reported by Li et al.[34] for a 2.4 mm aperture size lens. However, it is challenging to achieve a large aperture lens with only a concentric electrodes design because of the switching speed limitation. As seen from Eqs. (2) and (3), for a specific optical power and LC material, the thickness of the LC lens is proportional to the square of the lens radius ($d \propto R^2$). On the other hand, the response time in an LC cell is proportional to the square of the cell thickness ($\tau \propto d^2$).[35] As a result, a large area LC lens significantly increases the response time of the lens ($\tau \propto R^4$).

To reduce the limitation of the switching speed of the large aperture LC lenses, many approaches have been reported recently.[30,36–45] Among these approaches, the concentric ring electrode-based segmented phase profile (SPP) LC lens is continuously tunable, has a simple design, and maintains a parabolic phase profile within a large area.[30,36] In this design, the area of the segmented phase regions (SPRs) remains the same; as a result, the width of SPR changes in parabolic fashion. For a specific LC cell thickness, the OPD across a single SPR follows Eq. (2). By maintaining a specific cell thickness (d), the total number of SPP regions (N_s) for a specific lens aperture ® and focal length (f) is written as follows:

$$N_s = \frac{\mathrm{OPD}_{\text{ideal lens}}}{\mathrm{OPD}_{\text{LC}}}. \tag{5}$$

A schematic diagram of the LC director in the concentric electrode-based SPP lens is shown in Fig. 1(b); only two SPRs are shown for simplicity. By tuning the applied voltages on the discrete electrodes of each SPR, the optical power of the SPP LC lenses can be tuned.[36,46,47] If the phase difference between the adjacent SPR is a multiple of 2π radians, the maximum diffraction efficiency is achieved.[48,49] Figure 1(c) shows the optical path length (OPL) of an example SPP lens compared to an ideal parabolic phase profile lens. The red curve represents the ideal parabolic phase profile for the desired optical power, and the blue curve represents the LC lens phase profile utilizing the SPP method, which involves resetting the phase profile by $2\pi * 8$ radians at the boundary of each SPR. Basic design, modeling, and characterization of concentric electrode-based SPP lenses with an aperture size of 20 mm is reported by Jamali et al.[36] The same design principal was applied to achieve a larger diameter (50 mm) tunable lens; the optical characterization of the first prototype was reported recently, and the image quality degradation due to haze was observed.[4] The objective of this paper is to investigate the primary sources of haze in concentric electrode-based SPP lenses, propose solutions using simulation tools, and experimentally validate it through a fabricated prototype. This type of haze analysis has not been reported previously and is crucial for achieving tunable LC lenses with large apertures and excellent optical quality.

The main haze sources are related to two types of phase discontinuities. One of these phase discontinuities occurs at the edge of the electrodes, and the other occurs at the boundary of the segmented profile. In the following sections, both issues are discussed.

2 Problem of Haze Caused by Discrete Electrode Approach

The goal of a high-quality lens is to achieve a smooth change in phase. LC lenses using concentric ring electrodes typically have gaps between the rings to achieve a voltage divided circuit, which causes a disruption in the phase. To improve the phase continuity over the ring electrodes, Li et al.[34] demonstrated extra electrodes to cover the gaps between the rings, which created a more continuous phase profile. These added electrodes, known as "floating electrodes," are separated from the driving electrodes by a thin insulating layer (200 nm thick). As a result, the floating electrodes are capacitively coupled to driving electrodes and overcome the phase distortion at the electrode gap. Therefore, the phase profile is smoother compared with lenses without floating electrodes. To show the effect of the electrode gap in the presence of floating electrodes compared with no floating electrodes, the change of retardation color in two LC lenses are shown in Fig. 2. The discontinuity is clearly visible for the case of no floating electrodes in the gaps between the electrodes, indicated by the white arrow in Fig. 2(a). The use of floating electrodes shows a reduction of the phase discontinuity at the electrode gap region, which resulted in an improved image quality, as reported in a previous study.[34] However, with a closer look at the retardation color change on the LC lens with floating electrodes, it is observed experimentally [indicated by the white arrow in Fig. 2(b)] and from computer simulation (indicated by two red arrows in Fig. 6) that the previously reported process has an effect of causing a strong fringe field at the edges of the floating electrodes. As seen in Fig. 2(b), the implementation of floating electrodes reduces the disruption caused by the electrode gaps but creates a different problem at the edges of the electrodes. The edges of the floating electrodes create a bright edge on one side and a dark edge on the other side, which is a result of the optical effect of the fringing fields.

It is one objective of this paper to quantify and reduce the phase distortion related to the fringe fields at the edge of the floating electrodes.

3 Problem of Haze Caused by the Segmented Phase Profile

As discussed previously, lenses designed with an SPP are useful for reducing the thickness of the LC layer and the device response time. However, at the boundaries of each phase segment, there is a phase reset that degrades the lens performance. The issue is discussed in this section.

At any voltage level, the polar angle between the LC director and rubbing axis is defined as the LC director tilt angle. When the LC director changes the tilt angle with the applied voltage, the LC directors are expected to remain in the plane of the rubbing direction and electric field direction. However, at the phase reset boundary within a very narrow width between two adjacent electrodes, the applied voltage magnitude changes between two extreme values of voltage distribution (either lowest value to highest value or highest value to lowest value depending on the lens positive or the negative optical power[30]). Due to the concentric ring electrode

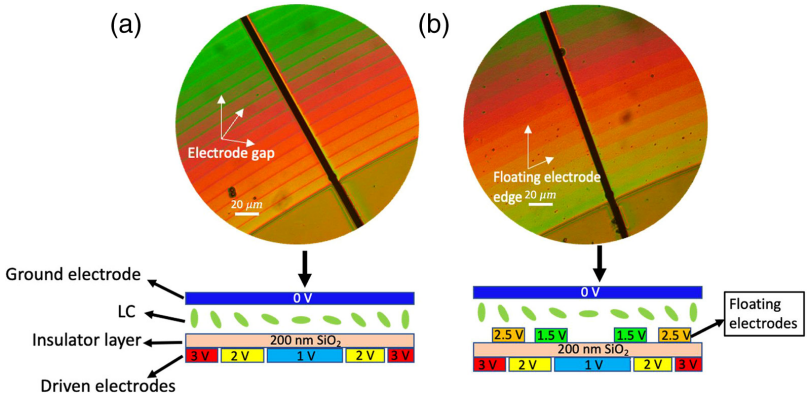

Fig. 2 Phase stepping and corresponding layer structure on the LC lens without floating electrode and with floating electrodes. (a) Retardation color change pictures of the built cells under cross polarizer without floating electrode. The white arrow shows the position of the 2 μm electrode gap. (b) With floating electrodes. The white arrow shows the edge of the floating electrodes.

structure, the direction of the fringing field between electrodes is radial. As a result, there will be areas of the lens where the radial fringing fields are either parallel or perpendicular to the rub direction. The maximum LC director distortion due to undesirable director twisting deformation occurs at the LC lens region where the radial direction is perpendicular to rub direction, and the maximum LC director distortion due to undesirable director bending deformation occurs at the LC lens region where the radial direction is parallel to the rub direction.

As an example case, the impact of the fringing field on phase resets is simulated (shown in Fig. 3) at the lens region where the tangent of the electrodes is parallel to the rubbing direction. The direction of the electric field within the LC cell is along the Z axis, and LC molecules are rubbed along the Y axis. As a result, LC directors are along the Y axis at a zero-voltage state. Figure 3(a1) shows the equipotential lines across to phase segments, and Fig. 3(b1) shows the resulting director profile. Figures 3(a2) and 3(b2) are the zoomed pictures of Figs. 3(a1) and 3(b1) around the phase reset. It can be seen that the fringing field in the X direction at the phase reset causes the director to rotate out of the $Y-Z$ plane. The width of the lateral distribution of the electric field as a result of the fringe field is indicated by the red double arrow in Fig. 3(a2), and distorted LC directors within the red double arrow region are highlighted in red in Fig. 3(b2). To understand the effect of the fringe field in the phase reset regions on the LC cell thickness, a director profile simulation is performed at different LC cell thicknesses, keeping the same reset and electrodes structures. From the result, we see that the director distortion width is approximately proportional to the LC lens cell thickness.

The LC director distortion at the phase reset region leads to a distorted phase jump at the resets [Fig. 4(a)] instead of an ideal phase jump [shown by the red dotted line in Fig. 4(a)], which affects the lens' optical performance by reducing its diffraction efficiency. If the director distortion width is considered to be the phase reset width, then the diffraction efficiency is written as follows:

$$\eta = \left(1 - \frac{\Gamma_d}{\Gamma_i}\right)^2, \tag{6}$$

where Γ_d represents the phase reset width and Γ_i represents the width of a particular SPR.[50] The phase reset width is related to the thickness of the LC cell and remains constant for a particular cell thickness, but the width of the SPP region decreases with the radius of the lens. Therefore, the diffraction efficiency of the LC lens also decreases along with lens radius. A comparison of the diffraction efficiency for LC lenses with cell thicknesses of 10, 20, and 30 μm for a 5 cm diameter LC lens with 28 phase resets is shown in Fig. 4(b). As the thicker LC cell causes wider

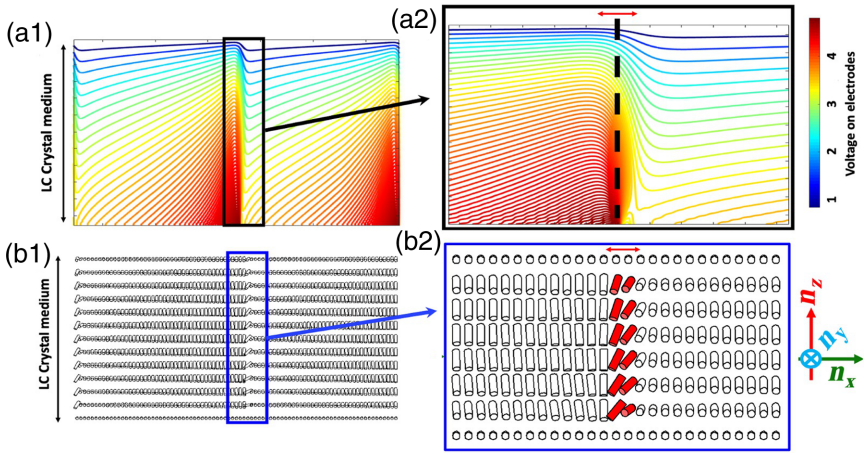

Fig. 3 SPP LC lens director simulation. (a1), (b2) Equipotential field line for voltage distribution over electrodes in the lens region with the SPP and corresponding director orientation within adjacent phase reset regions, respectively, in the $X-Z$ plane. Voltage magnitude on the patterned electrodes is shown in the color bar on the right. (a2), (b2) Zoomed view within rectangle area of (a1) and (b1), respectively.

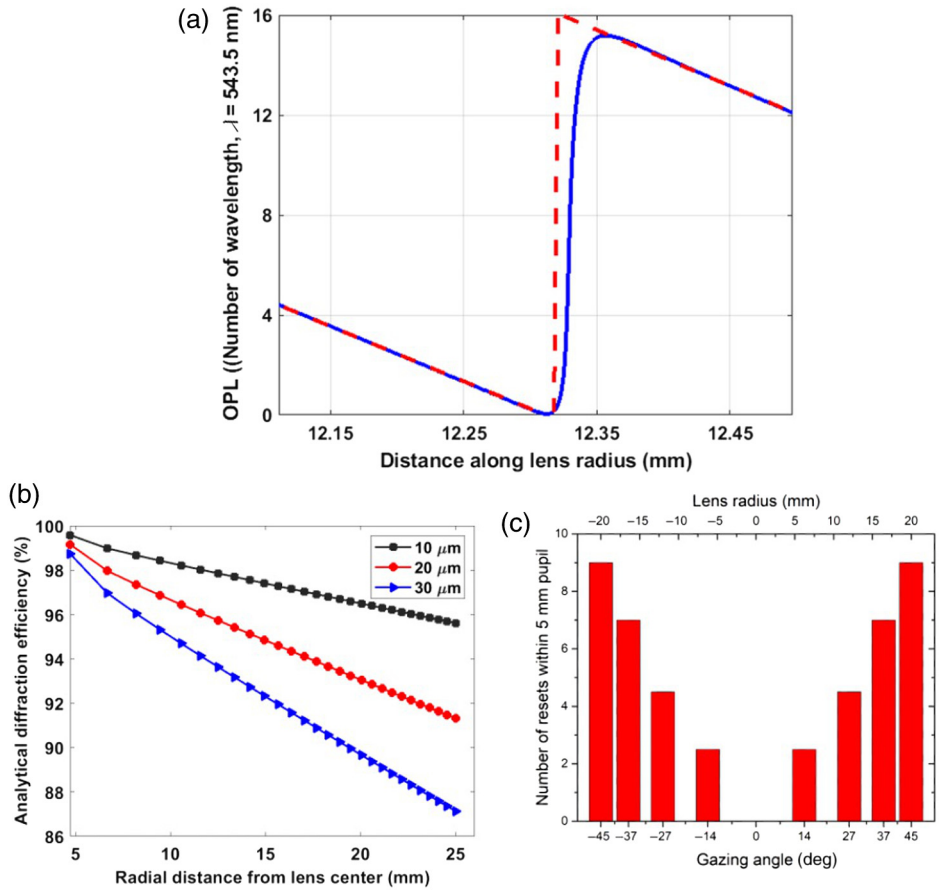

Fig. 4 (a) OPL of SPP LC lenses around the phase reset compared to ideal SPP type lenses (red dotted plot). (b) Change of analytical diffraction efficiency of 5 cm lens due to the LC director distortion for different LC lens cell thicknesses. (c) Change of number of resets within a 5 mm pupil diameter at different lens areas corresponds to different gazing angles from the center of the LC lens.

phase reset width, it can be seen that the diffraction efficiency drops significantly for thicker LC lenses for a given number of segmented phases on the lens design.

For near-to-eye applications, the haze performance will depend on the location where a user is looking through the lens surface. Taking the reference of average pupil size (5 mm) of the human eye,[51] the designed lens can be categorized by the number of phase resets over the 5 mm pupil aperture for different gazing angles. Considering the distance between the LC lens and the eye to be 2 cm, the density of phase resets within the 5 mm aperture of the eye is shown for five discrete locations on the lens area [Fig. 4(c)]. As the phase resets' density within a 5 mm pupil increases with the gazing angle, the amount of scattered light from the phase resets entering through pupil will increase toward the edge of the lens. Therefore, the light scattering will be more noticeable when the user gazes at a larger angle for the case of peripheral vision.

From the above discussion, it is clear that there will be haze generated by the reset regions of the SPP lens. Haze will be more noticeable when the user gazes at large angles through the periphery of the lens. It is the second objective of this paper to quantify and reduce haze due to this effect.

4 Methods

4.1 Example Concentric Electrode and SPP-Based Large Area (5 cm) LC Lens

Utilizing the SPP on the concentric ring electrode design, this paper considers calculated and experimental results of an example 5 cm diameter LC lens that is capable of tuning optical power from +0.80 to −0.80 D. As positive and negative optical power is possible, the total tunable

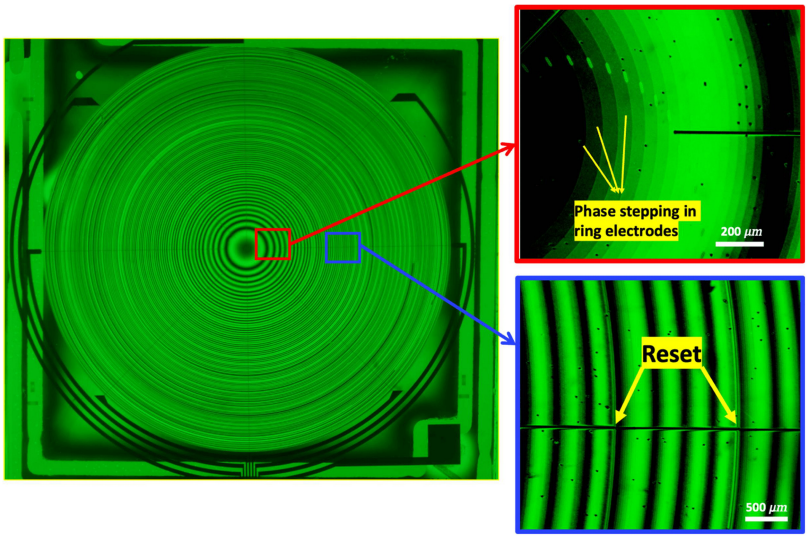

Fig. 5 Phase variation across the fabricated 50 mm aperture of the lens cell with the SPP design tuned for +0.20 D. The lens cell is placed at 45 deg between a cross polarizer, and the picture is taken with a green ($\lambda = 543$ nm) light filter. Red and blue square regions representing the zoom view of the center and off-center lens areas, respectively.

optical power range becomes 1.60 D. The design factors are similar to what was previously reported by Jamali et al.[36] To achieve ±0.80 D optical power, two LC lens cells, each capable of ±0.40 D, are optically stacked. These two stacked cells have an in-plane anti-parallel rubbing direction, which helps to improve the viewing angle performance.[52,53]

Following Eq. (3), the $\text{OPD}_{\text{ideal lens}}$ for ±0.40 D optical power lens with a 2.5 cm radius is equal to 125 μm or 230 λ (designed wavelength, $\lambda = 550$ nm), as shown in Fig. 1(c). However, as calculated from Eq. (2), to obtain an OPD_{LC} of 125 μm in an LC cell with 0.29 birefringence LC material, the required cell thickness is 431 μm. Such cell thicknesses require significantly longer time to switch the lens power, which is very unrealistic. However, with the inclusion of 28 SPP in the lens design, the requirement of the cell thickness is reduced. If we consider 75% of total the optical phase swing of 0.29 birefringence LC material, the required cell thickness of the SPP LC lens reduces to 20 μm, which helps to reduce the switching speed of the lens significantly. The switching speed of the discussed lens is reported to be <1 s.[46]

The fabricated lens is filled with the commercially available LC MLC-2172 from Merck, which has the following properties: $\Delta n = 0.2939$ ($n_e = 1.8139$ and $n_o = 1.5225$); dielectric anisotropy, $\Delta\varepsilon$ (at 1 kHz) = 13.4 ($\varepsilon_{\text{parallel}} = 17.8$ and $\varepsilon_{\text{perpendicular}} = 4.4$). The fabricated lens has a similar driving mechanism that has been described in previous papers.[4,34,47,52] The change in the refractive index of the LC lens is obtained by applying the voltage distribution in concentric ring electrodes connected with a resistive network. The tuned phase profile within the entire aperture of the fabricated prototype is shown in Fig. 5 for one optical power state; the phase discontinuity due to electrodes and resets is highlighted in this figure.

4.2 Modeling Method

The designed LC lens is analyzed using several calculation tools: the LC director relaxation method;[35] the finite difference time domain (FDTD) method to study wavetrain propagation through the designed LC lens and to calculate the near-field intensity versus the deflection angle;[54] and the scalar diffraction theory followed by Voelz[55] to obtain the spot profile intensity in the far field.

5 Reduction of Haze from the Edge of the Electrodes

The edge issue of the floating electrode is analyzed using LC director simulations with a voltage relaxation loop.[35] Due to the director distortion around the edge of the floating electrodes, the calculated OPL curve shows a phase bump at the edge of the floating electrode, indicated

by the red arrow in Fig. 6. It is observed that spacing between the LC layers from the electrode layer has an impact on the edge effect. Using the same LC material and same electrode structure, we have observed that the edge effect can be reduced by increasing the distance between the LC layer and the electrode layer. The increased distance between the electrodes and the LC layer effectively reduces the fringing field at the electrode edge. The calculated OPL of an LC lens with a reduced fringe field is shown by the red curve in Fig. 6.

Experimentally, to reduce the edge effect of the floating electrodes, an additional insulator layer of thickness close to 1000 nm [indicated in Fig. 7(a)] is added in the previously reported process.[35] Such additional insulator layer reduces the optical edge effect of the floating electrodes considerably [Fig. 7(a)] compared with the case without the addition of an insulator layer [Fig. 2(b)]. To compare the phase stepping over the ring electrodes, the change of the phase profile in terms of the number of waves is calculated against the electrode width and shown in Fig. 7(b) for the cases of no floating electrodes, with floating electrodes, and with floating electrodes including the additional insulator layer. It is observed that the LC cell structure without floating electrode shows a phase bump, whereas the LC lens structure with floating electrodes

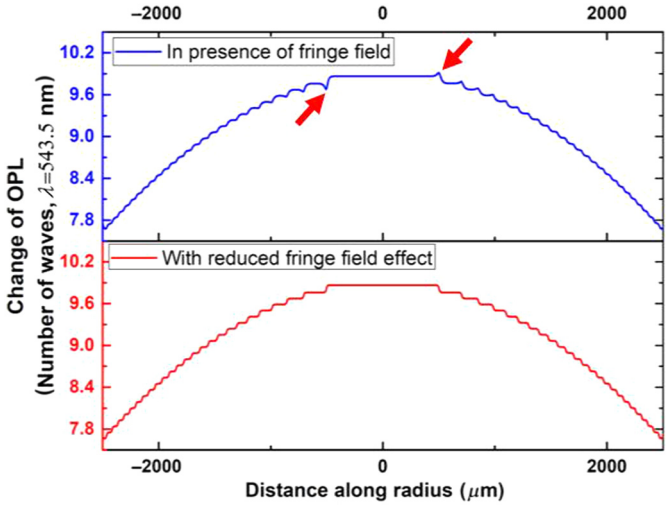

Fig. 6 Simulated OPL curve to study the fringe field effect on the ring electrode. The blue and red curves represent the change of OPL calculated from LC director orientation in the presence of fringing field effect and with a reduced fringe field effect, respectively.

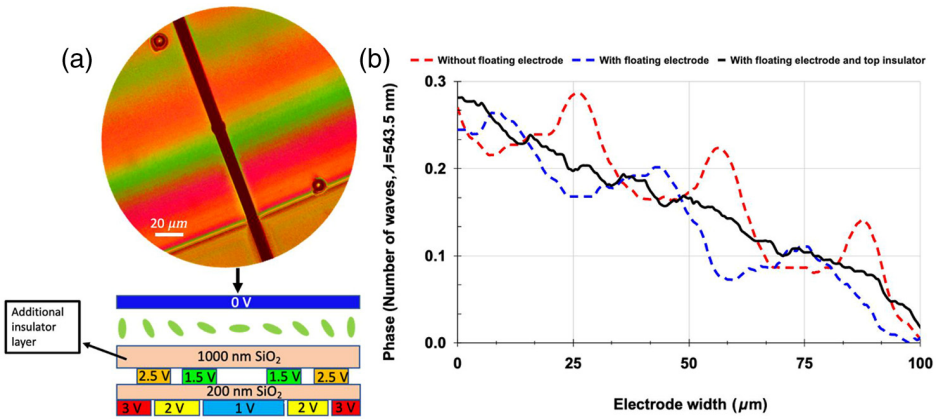

Fig. 7 (a) Phase stepping and corresponding layer structure on the LC lens with floating electrodes and top insulator layer. Change of color represents a change of retardation of the built cells under the cross polarizer. (b) Phase stepping over electrodes for the case of the LC lens cell without floating electrodes (red dashed curve), with floating electrodes (blue dashed curve) and with floating electrodes including the top insulator (black curve).

and the insulator layer on top of the electrode layer provides a more continuous change of phase retardation over the electrodes, which helps to improve the haze performance of the lens.

To quantify the floating electrode process optimization, imaging characterization using USAF 1951 chrome on a glass resolution chart is performed (Fig. 8). The USAF chart is illuminated by fluorescent light on the back and a polarizer is attached on top of the chart. The polarizer is aligned parallel to the rubbing direction of the LC lens. Images of the resolution chart are captured by a Canon Rebel XSI 450 D camera using 100 mm macrolens. To separate the haze contribution of the electrode edge effects from the haze contribution from the phase reset boundaries, imaging characterization in this section is only taken from the center of the LC lens within a 5 mm aperture, which does not include phase resets in the designed lens as shown in Fig. 1(c). When the LC lens is at the non-operating state, the image of the USAF chart is taken by the Canon camera; it is shown in Fig. 8(a). Figure 8(a) represents a defocused image. In Figs. 8(b) and 8(c), the fabricated LC lens is used to correct the defocus image by switching the optical power to +0.80 D. The image [Fig. 8(b)] captured through the LC lens that has a noticeable edge effect on the floating electrode shows more haze than the image [Fig. 8(c)] captured through the LC lens that has a reduced edge effect on the floating electrodes after process optimization using the top insulator. The optical quality improvement is quantified by measuring the contrast transfer function (CTF) using the equation:

$$\mathrm{CTF} = \frac{I_{\max} - I_{\min}}{I_{\max} + I_{\min}}, \tag{7}$$

where $I_{\max}$ and $I_{\min}$ are measured maximum and minimum green channel intensities around the group element of the USAF chart picture, respectively. The measured CTF at the center of the LC lens for different spatial frequencies is shown in Fig. 8(d), and the improvement in CTF is

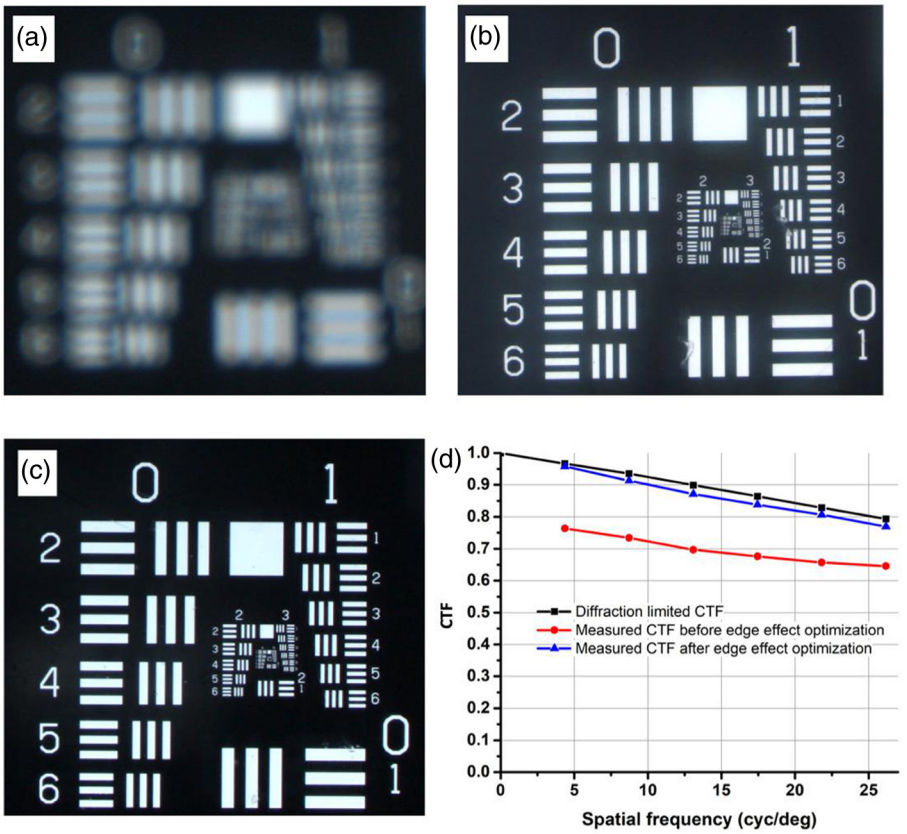

Fig. 8 Optical quality test at the center of the LC lens: (a) LC lens off. (b) LC lens on at +0.80 D with the non-optimized edge effect of the floating electrode. (c) LC lens on at +0.80 D with the reduced edge effect of the floating electrode after process optimization. (d) CTF comparison; the black, blue, and red plots represent the diffraction limited CTF, measured CTF after floating electrode process optimization, and measured CTF for non-optimized case, respectively.

observed. The measured CTF is close to the diffraction-limited case after reducing the edge effect of floating electrodes.

6 Reduction of Haze Due to Phase Resets in an SPP Lens

6.1 FDTD Study to Understand the Impact of LC Director Distortion at the Phase Reset Region at the Boundary Between Two Segmented Phase Regions

The impact of the director distortion due to the phase reset regions at the boundary between two SPRs on light propagation is studied using FDTD simulation. This simulation involves a wave train traveling from air medium through the LC layer, where the calculated LC director orientation is included. The outgoing wave train experiences a phase delay compared with the incoming wave train due to the variation in refractive index within the LC layer. In Fig. 9(a), a straight dashed blue line is used to compare the phase difference between different SPRs. It is seen that the phase difference between outgoing waves of one SPR relative to the other is equal to a multiple of 2π (zoomed view is shown within the pink figure inset). However, there is a phase disturbance within a narrow area in the reset region between the two SPRs, as indicated by the red line. It can be seen that the wavefront normal in the reset region is in the opposite direction and of a higher angle than the wavefront normal for waves from the SPRs. The resulting far-field intensity profile is shown in Fig. 9(b). The main diffraction peak in the far-field intensity profile corresponds to the phase difference of the outgoing wave train, shown in the yellow background

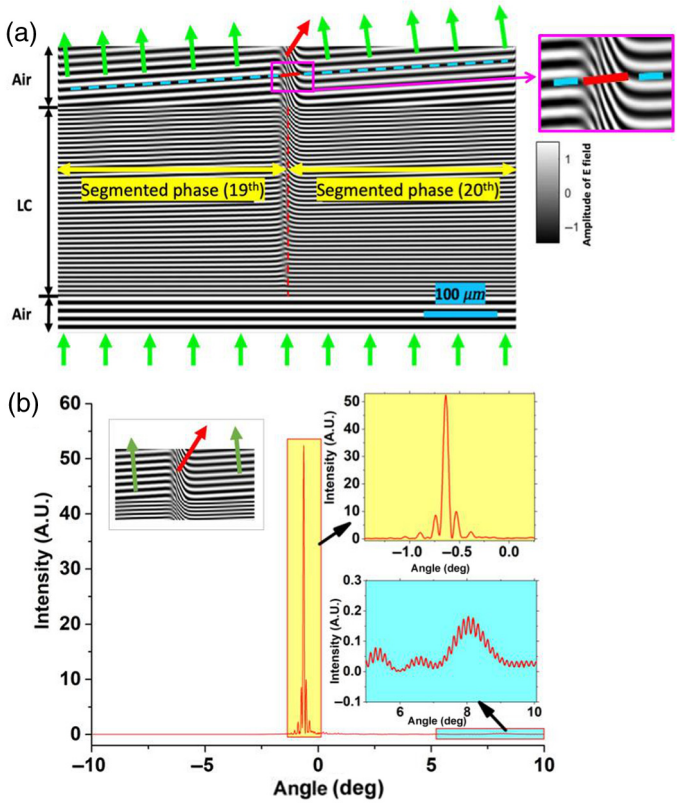

Fig. 9 FDTD study of calculated SPP LC lens. (a) Wave-train propagation through calculated LC director orientation at an incident light angle of 0 deg. The color bar on the right presents the change of amplitude of the propagating electric field. The green arrow indicates the rays that are propagating in the expected direction, and red arrow shows the undesirable light propagation from the phase reset boundaries. The red marked portion on top of the dashed blue line represents the width where phase disturbance is observed. The zoom view around the phase reset is shown within the pink box (b) simulated far-field spot profile of the SPP LC lens. Top and bottom subfigures on the right are zoomed portions of the regions that represent the main diffraction peaks and large angle diffraction peaks, respectively.

subplot in Fig. 9(b). However, due to the disturbance in the phase within the narrow region of the reset boundary, light deflects in an undesirable direction at a much larger angle, shown by a blue background subplot in Fig. 9(b). This results in small intensity peaks in the far field.

6.2 Close Distance Spot Profile Using Scalar Diffraction Analysis

For the near-eye application, close distance spot profile analysis is important. For this purpose, scalar diffraction analysis was performed on a designed +0.80 D LC lens at a close distance of 1 cm from the lens surface. At this near-field distance, the monochromatic light distribution from the 5 mm diameter circular aperture of the lens surface is recorded and shown in Fig. 10. It is observed that the intensity of the recorded light at the phase reset locations is reduced within a narrow region, indicated by orange arrows in Fig. 10. Such a reduction in intensity at the segmented phase boundaries leads to the amplitude grating problem. Additionally, there is an undesired light intensity distribution outside the aperture width (indicated by a red arrow in Fig. 10), which induces background haze and drops the contrast ratio.

6.3 Proposed Method for Reduction of Haze from the Phase Resets

In this section, a potential solution to reduce the effect of the director distortion around the phase reset boundary is proposed. As seen from the FDTD study (Fig. 9), light from the narrow width of the reset boundary is propagating at a larger angle and in the opposite direction from the lens deflection angle. To eliminate the effect of the large angle scattering from the phase reset regions, a light absorbing layer is designed and placed at their locations. The light absorbing layer is named the "black mask (BM)". With the addition of the BM, it is observed that the far-field intensity of light at a large positive angle reduces significantly without changing the pattern of the main diffraction peaks [the zoomed view is shown in the subfigures of Fig. 11(a) of the spot profile]. The BM at the reset boundaries absorbs the undesirable light scattering and improves the diffraction efficiency. The additions of the light blocking layers might have a negative effect on the diffraction efficiency due to the introduction of an amplitude grating with periodicity related to the width of the SPRs. However, the large angle of the diffracted light from the uncovered reset regions caused that effect before the introduction of the BM [as intensity drops in the phase resets width, shown in Fig. 10(b)], so there is no negative effect of adding it.

The diffraction efficiency is calculated by measuring the ratio of the area under the curve within main diffraction peak (deflection angle between −2 deg and 0 deg) to the area under the curve within the large area of the far field that includes all of the higher order diffraction peaks (deflection angle −10 deg to 10 deg). From this calculation, the diffraction efficiency improved from 84% to 92% with the implementation of the light absorbing layer on top of the reset region.

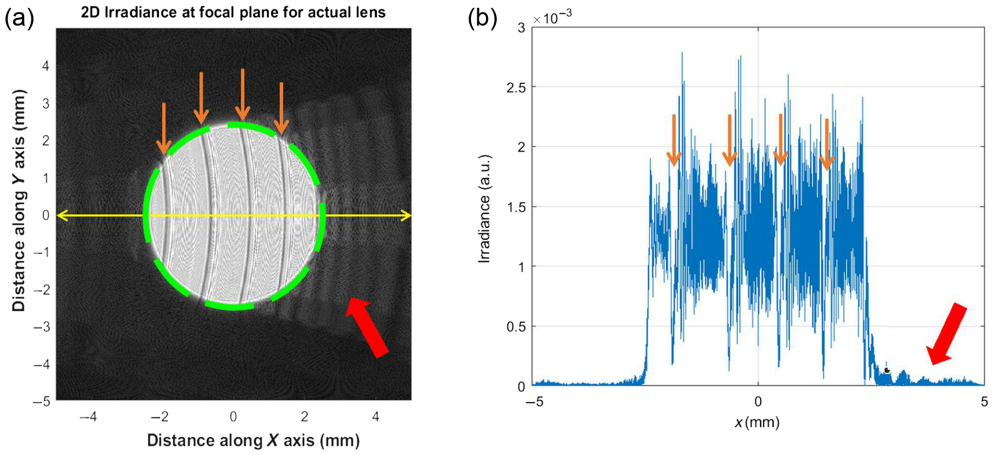

Fig. 10 Scalar diffraction analysis at a close distance from the LC lens. (a) Spot profile at the observation plane, where the light source aperture size, position of the phase resets, and scattered light are indicated by a green dashed circle, orange arrow line, and red arrow line, respectively. (b) Intensity variation along the yellow line of the spot profile shown in (a). The scattered light in the background is indicated by the red arrow mark.

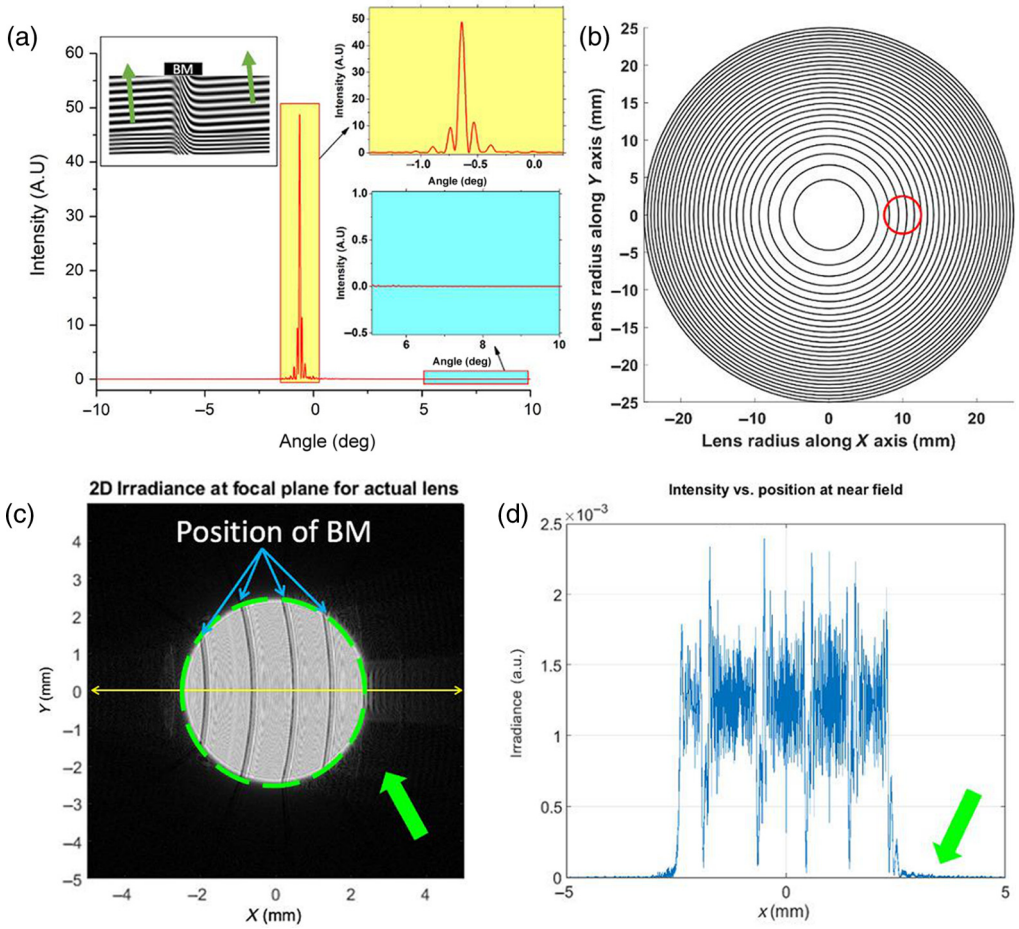

Fig. 11 Reduction of light scattering observed from the computer simulation. (a) Simulated far-field spot profile of the SPP LC lens from FDTD calculation. Top and bottom subfigures on the right are zoomed portions of the regions that represent the main diffraction peaks and large angle diffraction peaks, respectively. (b)–(d) Near-field simulation using scalar diffraction analysis. (b) The design lens SPP structure with a BM (black circles) and red circle on the structure represent the simulated region. (c) Near-field spot profile with a BM inclusion. (d) Intensity variation along the yellow line of (c).

The implementation of the BM in the near field is shown in Figs. 11(b)–11(d). Comparing Figs. 10(b) and 11(d), the reduction of the background light scattering (indicated by the green arrow) is observed with the inclusion of the BM.

6.4 Characterization of a Fabricated Device

This section describes the demonstration of the reduction of the light scattering effect with the implementation of a BM in a fabricated device. The positions of the BMs are centered on the phase distortion regions caused by the phase resets [shown in Fig. 12(a)]. In the fabrication process, the BM is aligned precisely in the location of the phase reset boundaries, which is highlighted in Fig. 12(b). The width of the BM in this study is 60 μm, whereas the predicted LC director distortion is ~20 μm due to the 20 μm LC lens cell thickness. Using scalar diffraction analysis, we see that the 60 μm width of the BM for the 20 μm thick LC lens cell gives the maximum absorbance of scattered light without affecting the main diffraction pattern. To observe the impact of the BM when voltage is applied, the image of a USAF chart is captured by a Canon Rebel XSI 450 D camera when light passes through the same area of the different LC lenses with a BM or without a BM. Figures. 12(c)–12(d) reflect the higher than normal exposure level image for the case of the LC lens without a BM and with a BM, respectively, at optical power +0.80 D. To capture the images of Figs. 12(c) and 12(d), two distinct LC lens samples (one with a BM and the other without a BM, respectively) are positioned without modifying the light illumination or

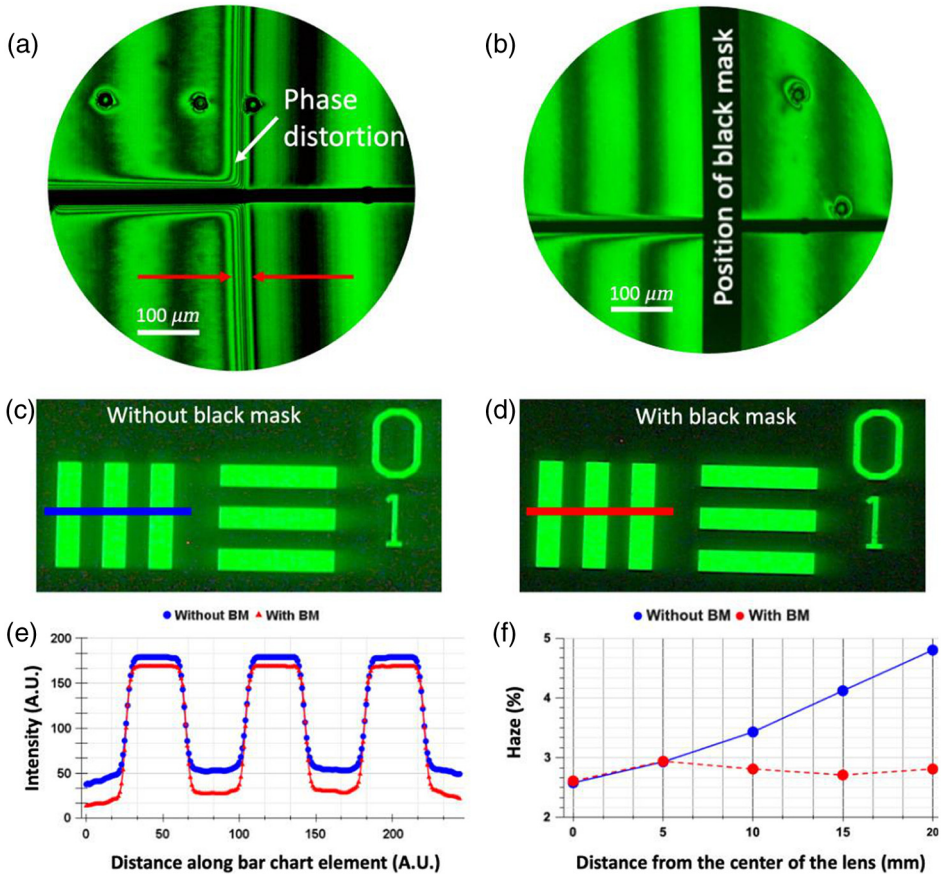

Fig. 12 Reduction of light scattering observed experimentally. (a) Closer look at the phase profile around reset boundaries on a fabricated lens, with phase disturbance indicated within the gap between red double arrows. (b) Position of the aligned BM on a fabricated device, the BM is covering the distorted phase region. (c), (d) The higher exposure picture of the USAF target for the LC lens without a BM and with a BM, respectively. (e) The intensity modulation around the group 0 element 1 for without a BM [taking intensity modulation along the blue line of (c)] and with a BM [taking intensity modulation along the red line of (d)]. (f) The haze (%) measurement on different lens locations for without a BM (solid blue line) and with a BM (dashed red line).

detector's imaging configuration. This ensures that the camera detector accurately records only the difference in the light scattering performance attributed to the presence of the BM. The reduction of light scattering is detected in the lens with a BM. The green channel intensity modulation is measured along the group element of the USAF chart picture and shown in Fig. 12(e). From the curve, it is observed that, with the inclusion of a BM, the bright level reduces by 5% and the dark level reduces by 40%, which implies an overall improvement of the contrast. To quantify the haze (%) due to light scattering from the phase reset boundaries with respect to the lens radius, a commercially available haze meter known as BYK haze gard i[56] is used. Two LC lens cells, which are characterized, have the same inner layer structures except that one of the cells has an additional BM. The samples are placed in the haze port of the haze meter, and light is passed through an aperture size of 4 mm to the integrated sphere. To measure haze (%) with respect to distance from the center of the LC lens, only the LC lens samples are translated in one direction without altering the haze meter calibration. At the LC lens "ON" state at optical power +0.80 D, as expected, it is observed that haze increases with the radial direction of the lens area for the case of without a BM; for the lens cells with a BM, the haze increases at some amount compared with haze at the center of the lens but remains constant at the off-center location on the lens surface [Fig. 12(f)]. Such a reduction of haze in the cells with a BM compared with those without a BM cell verifies the reduction of the LC director distortion effect in the SPP-based large aperture LC lenses.

7 Conclusion

In this paper, we have studied the haze effect of a concentric ring electrode-based GRIN tunable LC lens with an SPP design. The SPP design is promising for making large aperture tunable LC lenses without compromising the switching speed. As a result, such a lens has high potential in the field of AR/VR for solving AC mismatch issues, in ophthalmic applications or any imaging application. However, due to phase distortion at the phase resets and from the edge of floating electrodes, the light scattering effect degrades the optical quality of the lens. With the implementation of an insulator layer on top of the pattern floating electrodes, the concept of the reduction of haze from the edge of the electrodes is presented and experimentally verified. In addition, with the implementation of a BM on a designed lens, the concept of the reduction of the light scattering effect from the phase reset boundaries is presented and experimentally verified. Due to page restriction, the detail design, fabrication steps, and imaging characterization within the full field of view of the improved SPP LC lens utilizing the proposed haze reduction approaches is not presented in this paper; however, it is going to be the main goal of a follow-up publication.

Code, Data, and Materials Availability

Code and data not provided in the manuscript will soon be available in the dissertation of Amit Bhowmick with the advisor listed as Philip Bos from Kent State University or the ProQuest web site. The authors declare no conflicts of interest.

Acknowledgments

This project was funded by Meta Platform Inc., Reality Labs.

References

1. P. J. Bos et al., "28-2: Invited paper: simple method to reduce accommodation fatigue in virtual reality and augmented reality displays," *SID Symp. Digest of Tech. Pap.* **47**, 354–357 (2016).
2. A. Jamali et al., "LC lens systems to solve accommodation/convergence conflict in three-dimensional and virtual reality displays," *Opt. Eng.* **57**, 105101 (2018).
3. A. Jamali et al., "72-3: Design investigation of tunable liquid crystal lens for virtual reality displays," *SID Symp. Digest of Tech. Pap.* **48**, 1057–1060 (2017).
4. A. K. Bhowmick et al., "31-5: Student paper: liquid crystal based 5 cm adaptive focus lens to solve accommodation-convergence (AC) mismatch issue of AR/VR/3D displays," *SID Symp. Digest Tech. Pap.* **52**, 410–413 (2021).
5. Y.-H. Lin et al., "Liquid crystal lens set in augmented reality systems and virtual reality systems for rapidly varifocal images and vision correction," *Opt. Express* **30**, 22768–22778 (2022).
6. Y.-J. Wang and Y.-H. Lin, "Liquid crystal technology for vergence-accommodation conflicts in augmented reality and virtual reality systems: a review," *Liquid Cryst. Rev.* **9**, 35–64 (2021).
7. R. Stevens et al., "A review of adjustable lenses for head mounted displays," *Proc. SPIE* **10335**, 103350Q (2017).
8. T. Shibata et al., "Stereoscopic 3D display with optical correction for the reduction of the discrepancy between accommodation and convergence," *J. Soc. Inf. Disp.* **13**, 665–665 (2005).
9. A. Jamali et al., "Large area liquid crystal lenses for correction of presbyopia," *Opt. Express* **28**, 33982–33993 (2020).
10. M. Ye et al., "Properties of variable-focus liquid crystal lens and its application in focusing system," *Opt. Rev.* **14**, 173–175 (2007).
11. H. Ren and S. T. Wu, *Introduction to Adaptive Lenses*, p. 1–274, Wiley (2012).
12. A. K. Bhowmick et al., "Dynamic correction of astigmatism," *Appl. Opt.* **62**, 1791–1799 (2023).
13. D. Lanman and D. Luebke, "Near-eye light field displays," *ACM Trans. Graphics* **32**, 1–10 (2013).
14. Y.-M. Kwon, "Analysis of a head-mounted display-type multifocus display system using a laser scanning method," *Opt. Eng.* **50**, 034006 (2011).
15. G. D. Love et al., "High-speed switchable lens enables the development of a volumetric stereoscopic display," *Opt. Express* **17**, 15716–15716 (2009).
16. A. Maimone, A. Georgiou, and J. S. Kollin, "Holographic near-eye displays for virtual and augmented reality," *ACM Trans. Graphics* **36**(4), 1–16 (2017).
17. S. Barbero, "The Alvarez and Lohmann refractive lenses revisited," *Opt. Express* **17**, 9376–9376 (2009).
18. B. H. W. Hendriks et al., "Electrowetting-based variable-focus lens for miniature systems," *Opt. Rev.* **12**, 255–259 (2005).

19. H. Ren and S.-T. Wu, "Tunable-focus liquid microlens array using dielectrophoretic effect," *Opt. Express* **16**, 2646–2652 (2008).
20. N. Hasan et al., "Tunable-focus lens for adaptive eyeglasses," *Opt. Express* **25**, 1221–1221 (2017).
21. C. P. Chiu et al., "Liquid lenses and driving mechanisms: a review," *J. Adhes. Sci. Technol.* **26**, 1773–1788 (2012).
22. J. F. Algorri et al., "Recent advances in adaptive liquid crystal lenses," *Crystals* **9**, 272 (2019).
23. Y.-H. Lin, H.-S. Chen, and M.-S. Chen, "Electrically-tunable liquid crystal lenses and applications," *Proc. SPIE* **8642**, 86420C (2013).
24. H. Dou et al., "Large aperture liquid crystal lens array using a composited alignment layer," *Opt. Express* **26**, 9254–9262 (2018).
25. C.-J. Hsu, J.-J. Jhang, and C.-Y. Huang, "Large aperture liquid crystal lens with an imbedded floating ring electrode," *Opt. Express* **24**, 16722–16731 (2016).
26. C.-J. Hsu et al., "Influence of floating-ring-electrode on large-aperture liquid crystal lens," *Liquid Cryst.* **45**, 40–48 (2018).
27. G. Kramida, "Resolving the vergence-accommodation conflict in head-mounted displays," *IEEE Trans. Vision Comput. Graphics* **22**, 1912–1931 (2016).
28. Y. H. Lin, Y. J. Wang, and V. Reshetnyak, "Liquid crystal lenses with tunable focal length," *Liquid Cryst. Rev.* **5**, 111–143 (2017).
29. S. T. Kowel, D. S. Cleverly, and P. G. Kornreich, "Focusing by electrical modulation of refraction in a liquid crystal cell," *Appl. Opt.* **23**, 278–278 (1984).
30. G. Li et al., "Switchable electro-optic diffractive lens with high efficiency for ophthalmic applications," *Proc. Natl. Acad. Sci. U. S. A.* **103**, 6100–6104 (2006).
31. G. Li et al., "High-efficiency switchable flat diffractive ophthalmic lens with three-layer electrode pattern and two-layer via structures," *Appl. Phys. Lett.* **90**, 111105 (2007).
32. G. Li et al., "Large-aperture switchable thin diffractive lens with interleaved electrode patterns," *Appl. Phys. Lett.* **89**, 141120 (2006).
33. L. Li et al., "Near-diffraction-limited tunable liquid crystal lens with simplified design," *Opt. Eng.* **52**, 035007 (2013).
34. L. Li et al., "Near-diffraction-limited and low-haze electro-optical tunable liquid crystal lens with floating electrodes," *Opt. Express* **21**, 8371–8371 (2013).
35. D. K. Yang and S. T. Wu, *Fundamentals of Liquid Crystal Devices*, pp. 1–570, Wiley (2014).
36. A. Jamali et al., "Design of a large aperture tunable refractive Fresnel liquid crystal lens," *Appl. Opt.* **57**, B10 (2018).
37. J. N. Haddock, "Liquid crystal based electro-optic diffractive spectacle lenses and low operating voltage nematic liquid crystals," The University of Arizona (2005).
38. K.-T. Cheng et al., "Electrically switchable and optically rewritable reflective Fresnel zone plate in dye-doped cholesteric liquid crystals," *Opt. Express* **15**, 14078–14078 (2007).
39. Y.-H. Fan, H. Ren, and S.-T. Wu, "Switchable Fresnel lens using polymer-stabilized liquid crystals," *Opt. Express* **11**, 3080–3080 (2003).
40. Y. Li et al., "High efficiency multilevel phase-type Fresnel zone plates produced by two-photon polymerization of SU-8," *J. Opt. A: Pure Appl. Opt.* **12**, 035203 (2010).
41. O. Sova and T. Galstian, "Modal control refractive Fresnel lens with uniform liquid crystal layer," *Opt. Commun.* **474**, 126056 (2020).
42. X. Wei et al., "Multi-imaging characteristics of electrically controlled on-axis holographic polymer-dispersed liquid-crystal Fresnel lens," *Opt. Eng.* **54**, 037110 (2015).
43. N. Rong et al., "Polymer-stabilized blue-phase liquid crystal Fresnel lens cured with patterned light using a spatial light modulator," *J. Disp. Technol.* **12**, 1008–1012 (2016).
44. H. Ren, Y.-H. Lin, and S.-T. Wu, "Polarization-independent and fast-response phase modulators using double-layered liquid crystal gels," *Appl. Phys. Lett.* **88**, 061123 (2006).
45. H.-Y. Lin, N. Avci, and S.-J. Hwang, "High-diffraction-efficiency Fresnel lens based on annealed blue-phase liquid crystal–polymer composite," *Liquid Cryst.* **46**, 1359–1366 (2019).
46. A. Bhowmick et al., "Wide aperture (50 mm), compact, and high-quality continuous focus tunable gradient refractive index (GRIN) liquid crystal lenses," *Proc. SPIE* **12217**, 1221708 (2022).
47. A. K. Bhowmick et al., "Large aperture 0 D-2.5D tunable liquid crystal (LC) lens based on segmented phase profile for tunable focus application," *Proc. SPIE* **12023**, 1202303 (2022).
48. E. Hecht, *Optics*, Addison-Wesley (2001).
49. G. J. Swanson, "Binary optics technology: the theory and design of multi-level diffractive optical elements," Contract, pp. 1–53 (1989).
50. P. F. McManamon et al., "A review of phased array steering for narrow-band electrooptical systems," *Proc. IEEE* **97**, 1078–1096 (2009).
51. A. B. Watson, "A formula for the mean human optical modulation transfer function as a function of pupil size," *J. Vision* **13**, 18–18 (2013).

52. L. Li, D. Bryant, and P. J. Bos, "Liquid crystal lens with concentric electrodes and inter-electrode resistors," *Liquid Cryst. Rev.* **2**, 130–154 (2014).
53. L. Li et al., "Speed, optical power, and off-axis imaging improvement of refractive liquid crystal lenses," *Appl. Opt.* **53**, 1124–1131 (2014).
54. H. H. Cheng, A. K. Bhowmik, and P. J. Bos, "Concept for a transmissive, large angle, light steering device with high efficiency," *Opt. Lett.* **40**, 2080–2083 (2015).
55. D. G. Voelz, *Computational Fourier Optics: A MATLAB Tutorial*, SPIE Press, Bellingham, Washington (2011).
56. BYK haze-gard-i, https://www.byk-instruments.com/en/Appearance/haze-gard-Transparency-Transmission-Haze-Meter/Transparency-and-haze-meter/c/p-329.

Biographies of the authors are not available.